



HAL
open science

Geometry Induced Bias in the Remote Near-IR Identification of Phyllosilicates on Space Weathered Bodies

Stefano Rubino, Sandra Potin, Cateline Lantz, Donia Baklouti, Pierre Beck,
Olivier Brissaud, Hugues Leroux, Eric Quirico, Bernard Schmitt, Ferenc
Borondics, et al.

► **To cite this version:**

Stefano Rubino, Sandra Potin, Cateline Lantz, Donia Baklouti, Pierre Beck, et al.. Geometry Induced Bias in the Remote Near-IR Identification of Phyllosilicates on Space Weathered Bodies. *Icarus*, 2022, *Icarus*, 376, pp.114887. 10.1016/j.icarus.2022.114887. hal-03696309

HAL Id: hal-03696309

<https://hal.univ-lille.fr/hal-03696309>

Submitted on 22 Jul 2024

HAL is a multi-disciplinary open access archive for the deposit and dissemination of scientific research documents, whether they are published or not. The documents may come from teaching and research institutions in France or abroad, or from public or private research centers.

L'archive ouverte pluridisciplinaire **HAL**, est destinée au dépôt et à la diffusion de documents scientifiques de niveau recherche, publiés ou non, émanant des établissements d'enseignement et de recherche français ou étrangers, des laboratoires publics ou privés.



Distributed under a Creative Commons Attribution - NonCommercial 4.0 International License

Geometry Induced Bias in the Remote Near-IR Identification of Phyllosilicates on Space Weathered Bodies

Stefano Rubino¹, Sandra Potin², Celine Lantz¹, Donia Baklouti¹, Pierre Beck³, Olivier Brissaud³,
Hugues Leroux⁴, Eric Quirico³, Bernard Schmitt³, Ferenc Borondics⁵ and Rosario Brunetto¹

¹Institut d'Astrophysique Spatiale, Université Paris-Saclay, CNRS, F-91405, Orsay, France; stefano.rubino@ias.u-psud.fr

²Laboratoire d'Etudes Spatiales et d'Instrumentation en Astrophysique (LESIA), Observatoire de Paris, Université PSL, CNRS, Sorbonne Université,
Université de Paris, 5 place Jules Janssen, 92195 Meudon, France

³Université Grenoble Alpes, CNRS, IPAG, 414 rue de la Piscine, 38400 Saint-Martin d'Hères, France

⁴Univ. Lille, CNRS, INRAE, Centrale Lille, UMR 8207—Unité Matériaux et Transformations, F-59000 Lille, France

⁵SMIS Beamline, SOLEIL Synchrotron, Gif sur Yvette Cedex, France

Abstract

Sample return missions Hayabusa2 (JAXA) and OSIRIS-REx (NASA) found evidence of hydrated silicates on the surface of C and B-type asteroids Ryugu and Bennu. This detection relied on the study of the 2.7 μm OH-stretching spectral feature revealed from remote sensing observations of the asteroids' surfaces. Laboratory studies simulating the effects of space weathering (SpWe) on primitive bodies have shown that the feature's position, considered as the wavelength of the band minimum, can vary under ion implantation, shifting towards longer wavelengths for implanted surfaces. Since SpWe is a surface process, we investigated how the geometry of observation can affect the hydration feature on space weathered surfaces. Here, we report new laboratory Reflectance Factors (REFF) measurements on pristine and ion-bombarded phyllosilicate pellets, to monitor the evolution of the 2.7 μm feature with varying observation geometry. We found that, as we approach specular reflection, the feature's position for He⁺ bombarded surfaces shifts towards longer wavelengths. We interpret that the spectral shift is due to chemical and physical changes induced by ion implantation in the first hundreds of nanometers of our phyllosilicate pellets. The diversity in the observed amplitude of the shift means that different competing effects are dominating at different optical configurations, mainly volume and surface scattering. The effects of the ion-implanted matter are especially visible when measuring in near-specular conditions, where the specular component (more sensible to the very top surface (implanted layer) of the sample) dominates - hence the larger shift measured. Our results indicate that the geometry of observation can induce a certain bias in the interpretation of remote sensing data from space-weathered bodies.

¹ Corresponding author stefano.rubino@ias.u-psud.fr

1. INTRODUCTION

38 A correct interpretation of the hydration features on small bodies is paramount in understanding
the evolution of primitive materials in the early Solar System. It is particularly relevant in the
40 context of the two sample-return missions Hayabusa2 (JAXA) and OSIRIS-REx (NASA),
targeting the C-type asteroid (162173) Ryugu (Watanabe et al. 2017) and the B-type asteroid
42 (101955) Bennu (Lauretta et al. 2017), respectively. Hayabusa2 successfully collected material
from the surface of its target first in February 2019, then in July 2019, and brought back several
44 grams of Ryugu grains to the Earth, on Dec. 6 2020. OSIRIS-REx has also performed sample
collection from its target's surface in October 2020, and the spacecraft is now in the next phase
46 of the mission, Earth Return Cruise, starting in March 2021. Besides sample collection, both
missions performed extensive spectroscopic surveys in both the visible and the near-IR of their
48 target's surfaces, using the NIRS3 (Near Infrared Spectrometer, (Iwata et al. 2017) and OVIRS
(OSIRIS-REx Visible and InfraRed Spectrometer, (Christensen et al. 2018) instruments,
50 respectively. They detected a band at $2.72 \mu\text{m}$ on Ryugu (Kitazato et al. 2019) and at $2.74 \mu\text{m}$
on Bennu (Hamilton et al. 2019), associated with the stretching vibration of hydroxyl groups
52 (-OH) covalently bonded to metallic atoms (M) in phyllosilicates. The position and the shape
of this hydration feature can vary with mineral composition and structure (Madejová, Gates,
54 and Petit 2017). The $2.7 \mu\text{m}$ feature has been studied in carbonaceous chondrites (Takir et al.
2013), but it has also been detected on outer space bodies, such as the dwarf planet Ceres (De
56 Sanctis et al. 2015) and some other low-albedo objects (such as C-class and related asteroids -
(Jones et al. 1990; Usui et al. 2018; Rivkin et al. 2002). On Bennu, the feature appears to be
58 deep and broad, similar in shape to laboratory spectra of some carbonaceous chondrites.
However, Ryugu's feature is significantly weaker and narrower, indicating a different degree
60 of surface hydration and/or a different thermal history (Kitazato et al. 2021). Hayabusa2 also
conducted an impact experiment using the Small Carry-on Impactor (SCI). Results are
62 described by (Arakawa et al. 2020) and the subsurface material NIRS3 observations are
presented by (Kitazato et al. 2021). The excavated material exhibits a $2.7 \mu\text{m}$ feature that
64 appears stronger and slightly blueshifted in comparison to the one observed for the surface.
Space weathering (SpWe) could explain these observations: SpWe affects atmosphere-less
66 bodies in our solar system by multiple processes, such as micrometeorite bombardment, high-
energy cosmic irradiation and solar wind bombardment, with both high and low energy ions
68 (Beth Ellen Clark et al. 2002; Brunetto et al. 2015). SpWe can alter the physical and chemical
structure of surface materials on asteroidal bodies, inducing variations of their spectral

70 properties (B. E. Clark et al. 2001; Ishiguro et al. 2007). Recent attempts to reproduce solar
wind SpWe in the laboratory, both on carbonaceous chondrites (CCs) (Lantz et al. 2015, 2017;
72 Brunetto et al. 2020) and on hydrated terrestrial silicates (Rubino et al. 2020), have shown that
the $2.7 \mu\text{m}$ feature in native hydrated silicates appears at shorter wavelengths than in ion-
74 bombarded samples, similarly to the observation by NIRS3 on the SCI crater on Ryugu.
However, recent studies have shown that the geometrical configuration of an observation can
76 affect the shape of the hydration feature in carbonaceous chondrites (S. Potin et al. 2019).
Remote sensing instruments onboard space missions often observe objects at different times
78 and angles, in a way that the same area is measured at various geometries. Thus, it is important
to investigate and understand how the geometry of the observation can affect the hydration
80 feature on space weathered surfaces. To address this question, we report new experimental
Reflectance Factor (REFF) measurements on pristine and ion-bombarded phyllosilicate pellets,
82 aimed at monitoring the evolution of the $2.7 \mu\text{m}$ feature with varying observation geometry.

84 2. SAMPLES AND METHODS

86 2.1 Samples description and preparation

The new REFF measurements were done on the phyllosilicate pellets used by Rubino
88 et al. (2020), which underwent He^+ and Ar^+ ion bombardment at 40 keV , at room temperature
and $P \sim 10^{-7} \text{ mBar}$, with an ion fluence of $6 \cdot 10^{16} \text{ ions/cm}^2$ for He^+ and $2 \cdot 10^{16} \text{ ions/cm}^2$ for
90 Ar^+ . The relevance and the limitations of He^+ and Ar^+ ion-bombardment at 40 keV as a
simulation of solar wind irradiation are presented in the paper preceding this work, Rubino et
92 al. (2020), and further discussed by Brunetto et al. (2014) and Lantz et al. (2017).

The measurements presented in this work were performed on a serpentine sample.
94 Serpentine is among the major hydrated silicates phases found in CI- and CM-type
chondrites (King et al. 2015) and can be used as analogs for the surface of primitive hydrated
96 bodies such as Ryugu and Bennu (Kitazato et al. 2019; Hamilton et al. 2019). Our serpentine
was extracted from the Rawhide mines, in California. It will thus be referred to as Serpentine
98 Rawhide. This sample is mostly antigorite with chrysotile veins, with a $\text{Fe}/(\text{Fe}+\text{Mg})$ ratio equal
to 0.07 .

100 The sample was crushed using an agate mortar. The grain size of the resulting powder
was estimated by scanning electron microscopy (SEM), and was found in the range $1\text{-}100 \mu\text{m}$.
102 Three pellets were made by pressing $\sim 240 \text{ mg}$ of powdered sample onto a PEG substrate

(powdered polyethylene glycol with an average molecular mass of 8000 g/mol , from Fisher Scientific), for a duration of 5 minutes, using a 7-tons press. We made three pellets, two of them underwent ion-bombardment, while the third/last pellet was preserved as a control sample. The pellets have a somewhat flat surface, which is expected to produce strong specular effects. Additional details about the samples and sample preparation can be found in Rubino et al. 2020.

It is relevant to note that meteorites are generally used as analogue materials for asteroidal surfaces. And in fact, ion-implantation experiments have already been conducted on meteorites (see Brunetto et al. 2014, Lantz et al. 2015-2017). However, meteorites can also be very heterogeneous materials, especially at the scale we are working here (mm to fractions of microns). This heterogeneity may introduce other effects in our measurements, which may not be well constrained. This may hinder the efforts in deriving a sort of "general behavior" of hydrated silicates under ion-bombardment, hence the choice in this work of focusing on pure (or almost pure) phyllosilicate phases.

2.2 Experimental setup

2.2.A Reflectance Factor (REFF)

We performed the REFF measurements with the SHADOWS (Spectrophotometer with cHanging Angles for the Detection Of Weak Signals) spectro-gonio radiometer at the Université of Grenoble Alpes (Sandra Potin et al. 2018). This instrument allows acquiring spectra in the visible and near infrared range ($350\text{-}5000 \text{ nm}$) at different observation geometries. A monochromatic beam is focused on the sample's surface, with beam-size of approximately 5.2 mm in diameter for a nadir illumination (normal to the surface). The reflected light is measured by two detectors, covering the visible and near-infrared ranges, mounted on a rotating arm. The illumination and the observation angles are defined with respect to the normal to the surface and can be changed, which allows us to automatically acquire spectra for different observation geometries. For our measurements, we set four illumination angles : 0° , 20° , 40° and 60° , with an angular resolution of $\pm 2.9^\circ$. For each illumination angle, we acquired a series of spectra by varying the observation angle, from -70° to 70° , with a 10° step and an angular resolution of $\pm 2.05^\circ$, exploring all geometrical configurations except opposition geometry. For each sample, using these parameters, a total of 56 geometrical configurations were explored. The spectral sampling and the evolution of the spectral resolution in our spectra are shown in appendix A. This parameter set configuration resulted in approximately 13h of acquisition per sample. The reflectance factor is calculated during the measurement by

comparison with a Spectralon (99% reflectance, Labsphere) and Infragold (Labsphere) reflectance targets, taking into account the Reflectance Factors (REFF) of the references, meaning that the reference is measured at the same observation geometry of the sample. The reflectance of the samples is thus compared to a lambertian surface, by dividing the measured spectra with the reference spectra. In this configuration, reflectance values above 1 for specular configuration on very flat surfaces are to be expected.

2.2.B Scanning Electron Microscopy imaging

After spectroscopic measurements, Scanning Electron Microscopy SEM studies were conducted at the University of Lille, France. A thin coating of carbon was deposited over the pellet surface to perform high resolution secondary electron imaging at 3 keV, using a JEOL JSM-7800F at a working distance of *10 mm*. High magnification images of the pellets' surfaces were acquired to visualize changes in the surface topography due to ion implantation.

3. RESULTS

3.1 Main spectral features

Almost all the acquired spectra show the same absorption bands (shown in Figure 1):

- ❖ a deep 2.7 μm band associated as with the (M)-OH stretching vibration ;
- ❖ a broad 3 μm shoulder, which can be a combination of structural and adsorbed water bands (in this sample, minor amounts of structural water are expected, so this contribution is probably dominated by the contribution of adsorbed water) , as well as CH stretching bands around 3.4 μm ;
- ❖ overtones and combination mode peaks of water molecules at 1.4 and 1.9 μm (Ryskin 1974; Ockman 1958) ;
- ❖ two additional bands at 2.3 and 2.5 μm , originated from the stretching vibrations of Mg-OH and/or Fe-OH (Clark et al. 1990).

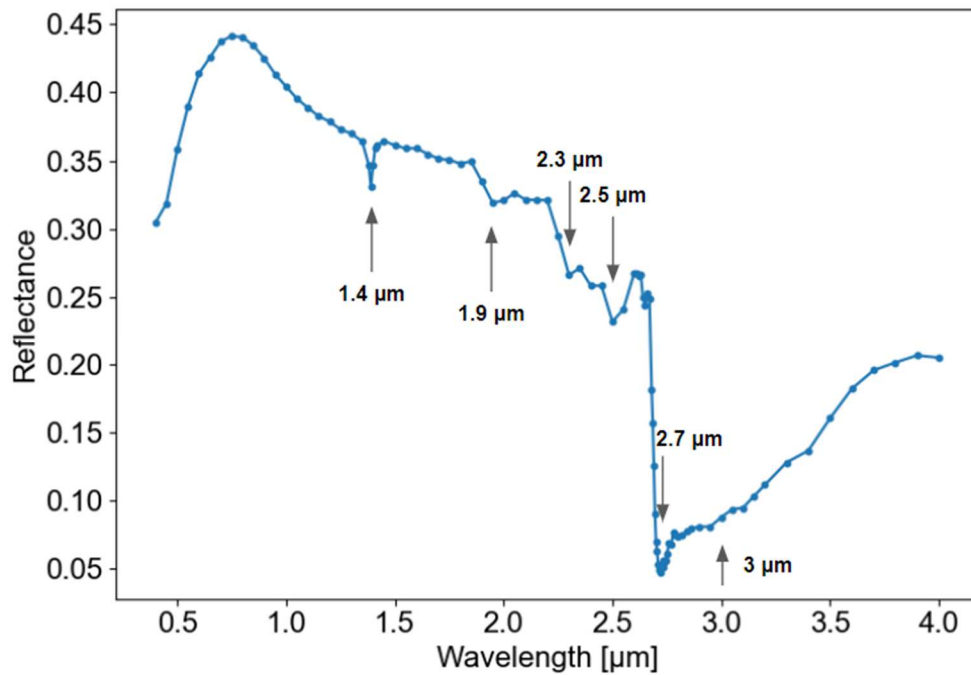


Figure 1. Example of acquired spectra – He^+ implanted pellet at $(i, e) = 20^\circ, 40^\circ$

164

166

168 Generally speaking, the first effect we notice is a change in the shape of the hydration
 170 band at $2.7 \mu m$, which gets sharper as we approach the specular reflection geometry (see Figure
 2). For some configurations, when looking at the whole dataset (see Appendix B, figure B1),
 approaching specular geometry, strong features seem to sharpen while less intense ones seem
 to shrink.

172

We also note that due to a possible increase of the contribution from specular reflection,
 spectra from these configurations also could exhibit the spectral signature of the real refractive
 index from the top layer. This can happen because the real part of the refractive index n always
 oscillates like a derivative around a band (see Kramers-Kronig relations -) and is always lower
 before the band peak and higher after: thus the specular contribution is lower and then higher.
 This induces a negative (or blue) shift of the 'apparent absorption' peak position when added
 with the multiple scattering contribution. This signature would corresponds to the slight bump
 after the $2.7 \mu m$ feature (at approximately $2.715 \mu m$), and the tiny blue-shift of the $2.7 \mu m$
 band, visible in the non-bombarded sample (the position of the feature shifts from $2.705 \mu m$
 for $[i = 60^\circ, e = 0^\circ]$ to 2.700 for $[i = 60^\circ, e = 60^\circ]$ - note that the spectral sampling here
 corresponds to $5 mm$). For reference, the complex refractive index spectrum in serpentines to
 illustrate the optical constant's behavior can be found in Mooney and Knacke (1985).

184

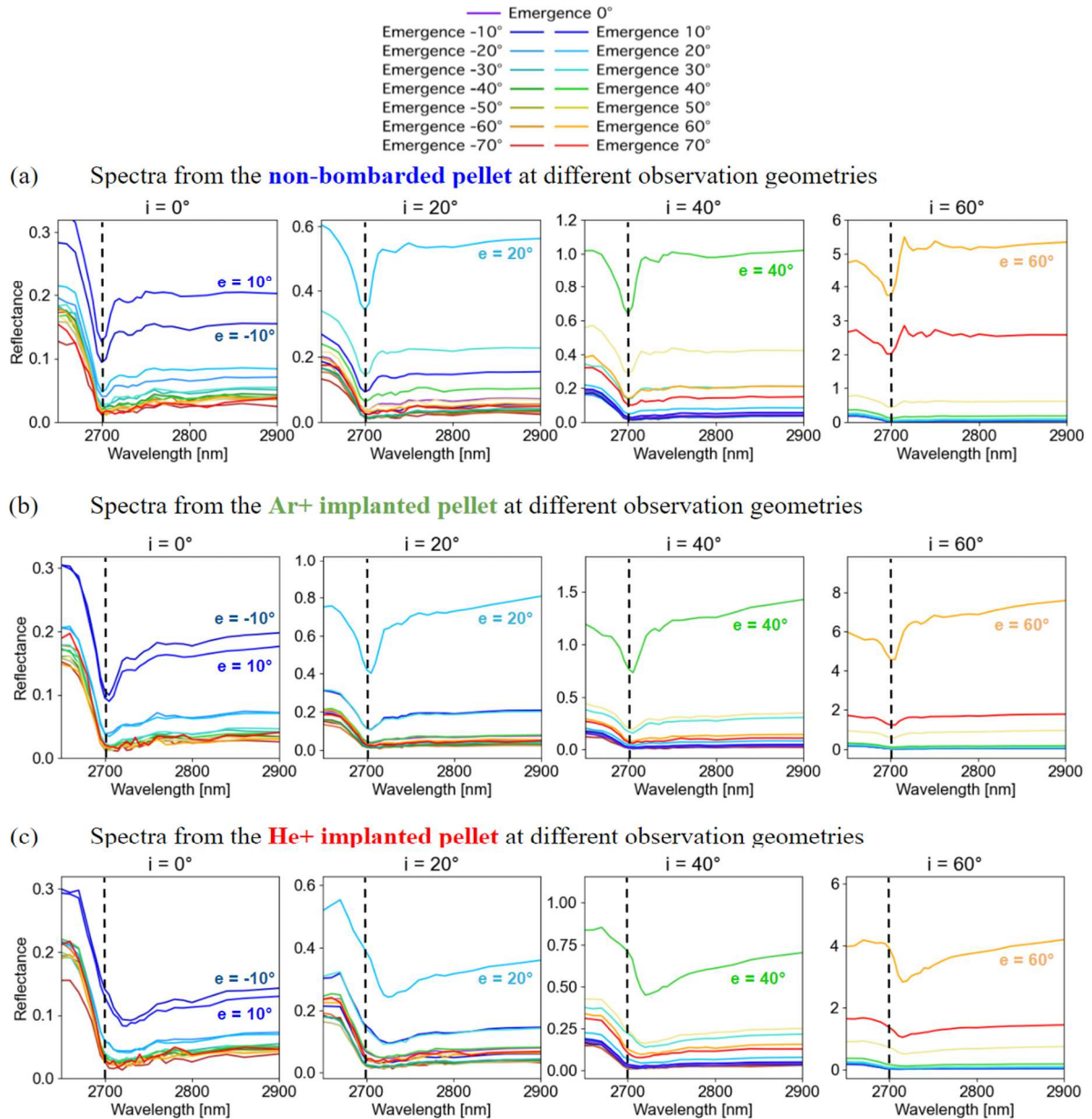
Delving a bit deeper, while focusing on the hydration band, different behavior can be
 seen for the different cases :

186
188
190
192
194
196
198
200

- ❖ For the non-bombarded sample, the most prominent effect is the change in the shape of the hydration band. Approaching near-specular configuration, the feature gets sharper. Moreover, as the incidence angle i grows, for large phase angles, the apparent blue-shift due to the influence of the optical constants described above get more notable ;
- ❖ For the Ar^+ bombarded sample, the sharpening effect described above can also be seen in near-specular configurations. The slight shape change effect due to the influence of the optical constants is also noticeable for the $i = 60^\circ$ case, although less intense ; there also seems to be a slight band position variability of the hydration feature (see section 3.2 for a detailed explanation);
- ❖ For the He^+ bombarded sample, the shape of the hydration band isn't affected by observation geometry as strongly as in the cases described above (or even at all) ; however, we can see a clear global band red-shift in the position of this band with respect to the other samples. The extent and evolution of this shift is further discussed in section 3.2.

202 These effects are better seen in the complete dataset, shown in Appendix B. We note that for
204 all observations of the ion implanted samples in particular geometric configurations, the shape
and position of the hydration feature can be considerably altered (Figure 2, panel c) with respect
to the non-implanted pellet (Figure 2, panel a).

206
208 Finally, we note that the curves in panel (a) of Figure 2 are fairly asymmetric with respect to
the emergence angle. This may be due to slight uncertainty in the position of the detector and
slight differences on the observation spot position for symmetric emergence angles, possibly
210 coupled to some lateral heterogeneity of the sample.

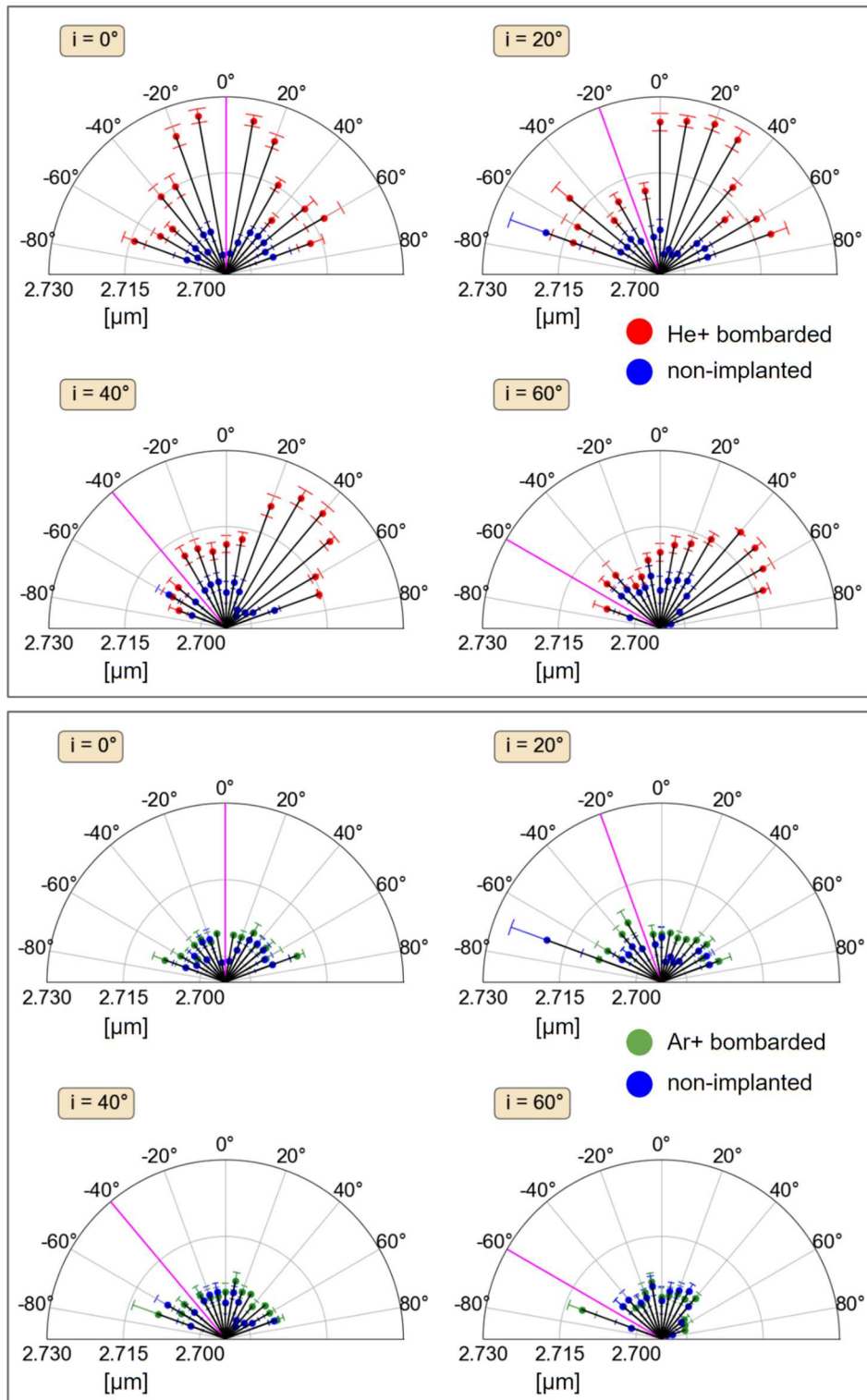


212 Figure 2. Detail of the REFF measurements centered around the hydration band (complete dataset but restricted
 214 to 2.65-2.9 μm). The dashed line is precisely at 2.7 μm , and is used to gauge the evolution of the 2.7 μm feature's
 position.

216 3.2 REFF dataset results

218 We quantified the changes of the hydration feature at 2.7 μm with varying optical
 geometries. To determine the two spectral parameters of interest, the peak position and the
 band depth, we applied the same method as in our previous work (Rubino et al. 2020). We first
 220 removed a linear continuum from 2.6 to 4 μm . The continuum-removed spectra, centered on
 the hydration feature, are shown in the Appendix B, Figure B2. We then applied different
 222 instances of a Savitzky-Golay filter, using different windows-size values, to slightly smooth
 our data while taking in account different band shapes and degrees of noise correction. For

224 each smoothed spectrum, we defined a region of interest (ROI) centered on the band and
computed the barycenter associated to this spectral ROI to account for the asymmetry of the
226 spectral feature. Finally, we averaged the wavelength obtained on each Savitzky-Golay
instance and associated this value with the band position. Since the Savitzky-Golay filter acts
228 as a sort of data interpolation process, by taking in consideration multiple instances of it, the
computed positional value is very precise, with an improved accuracy with respect to spectral
230 sampling and resolution (which still need to be taken in account when discussing the overall
accuracy of the measurement). This method allowed us to extract the band position for all
232 observation geometries. The band depth is calculated as $1 - R_{\text{Band}}/R_{\text{Continuum}}$, at the wavelength
corresponding to the center of the band, and considering a linear continuum between the two
234 inflection points of the band. The position values are shown in the polar plots of Figure 3.



236

238

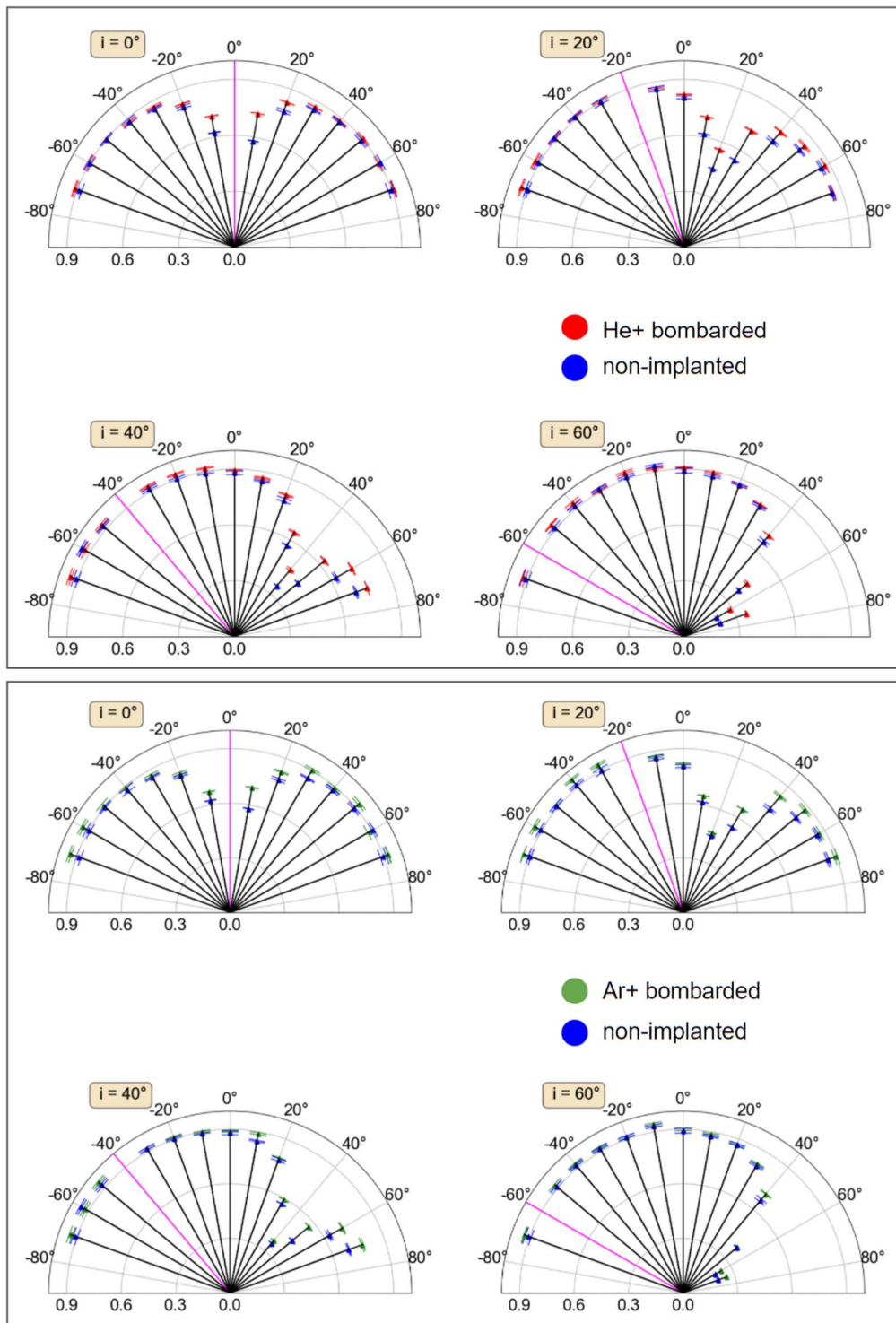
240

242

Figure 3. Evolution of the $2.7 \mu\text{m}$ hydration feature position under different optical geometries for He^+ and Ar^+ implanted pellets, with respect to the non-implanted pellet. The magenta line represents the direction of the illumination angle i . The plot shows the evolution of the $2.7 \mu\text{m}$ peak position as a function of the observation angle e , for fixed illumination angles i . In the polar plots, the observation angle e increases clockwise, while the illumination angle i increases counter-clockwise (scale not reported). The data from the ion implanted pellets (red for He^+ and green for Ar^+) are compared with data from the pristine pellets (in blue).

244 For the He^+ implanted pellets, the irradiation-induced spectral shift at longer wavelengths can
be seen in all optical configurations. The amplitude of this shift can vary from a few nanometers
246 to a maximum of $28 \pm 2 \text{ nm}$. The maximum is reached when observing in a specular
configuration, with an angular width of about $\pm 20^\circ$ (i.e., $e \sim i \pm 20^\circ$). It is interesting to
248 observe that for the large illumination angles, $i \sim 40^\circ$ and 60° , the spectral shifts increase also
when $i \sim -e$: this might possibly be suggestive of backscattering effects. For the Ar^+ -implanted
250 pellets, the spectral shift at longer wavelengths with respect to the non-bombarded sample is
less pronounced and can only be observed in specular configurations, where its amplitude is
252 close to 6 nm . Overall, the spectral resolution of our dataset does not allow us to efficiently
distinguish between an Ar^+ implanted pellet and a pristine one in most non-specular optical
254 configurations. Looking at the positional data from the non-bombarded pellet, we can also spot
the effect described in 3.1, where for specular geometries the specular component start to
256 dominate the spectra, and the spectral signature from the real refractive index can be seen
affecting the peak position, slightly blue-shifting it in these configurations. The evolution of
258 the $2.7 \mu\text{m}$ band depth (Figure 4) was also measured in a similar manner to the band position.
It is relevant to note that commenting band-depth value in reflectance spectra on particularly
260 bright surfaces can be quite delicate. As discussed by Milliken et al. (2007), band depth and
apparent absorbance values can be correlated to albedo when derived from reflectance spectra.
262 In the case of our study, the direct measure of band depth can be biased, especially approaching
specular configurations, due to the measured albedo. This complicates the interpretation of this
264 spectral parameter. However, this study highly focuses on the position of the hydration feature
and its evolution upon ion-implantation. Results on band-depth are still reported here.

266



268

270

272

274

Figure 4. Evolution of the $2.7 \mu\text{m}$ hydration feature depth under different optical geometries for He^+ and Ar^+ implanted pellets, with respect to the non-implanted pellet. The magenta line represents the direction of illumination which corresponds to the incidence angle.

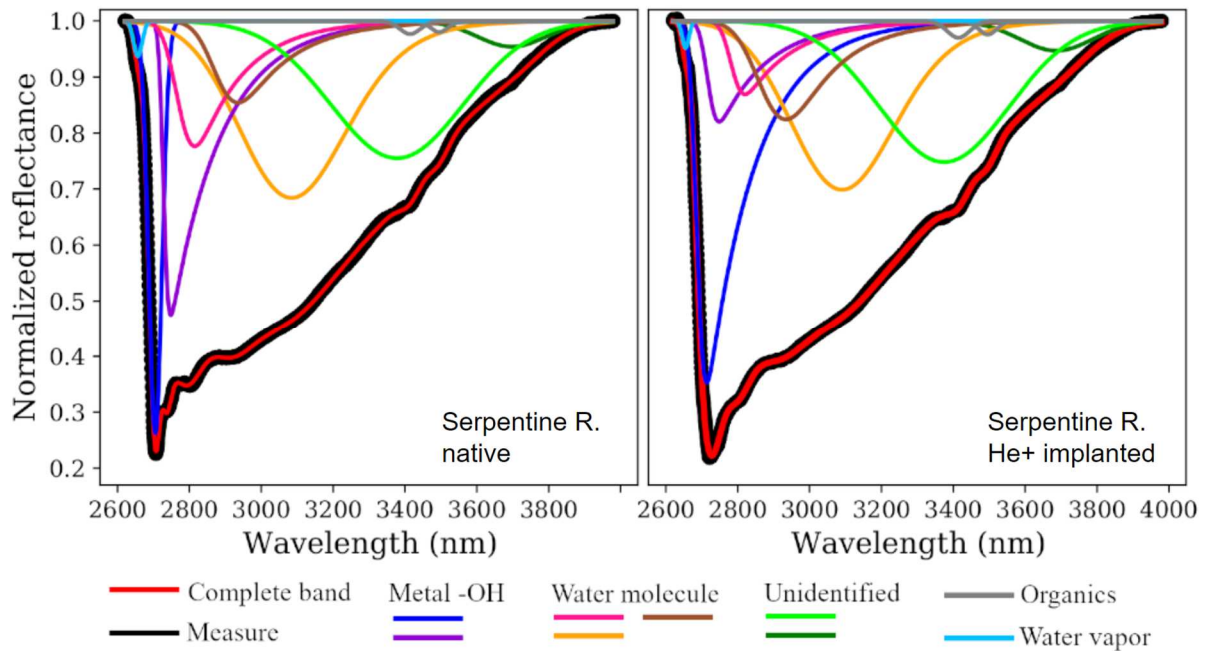
For all pellets, the $2.7 \mu\text{m}$ band depth decreases in amplitude when approaching the specular configuration. For a fixed geometrical configuration, the hydration feature measured on both the implanted pellets is deeper than for the pristine pellet. In specular configurations (or

276 approaching specular-like, for $i = 0$), the $2.7 \mu\text{m}$ band depth in the He^+ implanted pellets is
 ~30% deeper than in the pristine pellet. In the Ar^+ implanted pellets, the band intensity is only
 278 ~15% deeper than in the pristine pellet.

280 3.3 EMG modeling findings

It is important to address that the hydration feature in phyllosilicates can incorporate
 282 multiple contributions depending on the complexity of the phyllosilicate sample. Structural and
 adsorbed water can also have a spectral signature near $3 \mu\text{m}$, which can contribute to the broad
 284 spectral band at $3 \mu\text{m}$. The quantification of these contributions and their evolution can be
 accessed by Exponentially Modified Gaussian (EMG) modeling (Grushka 1972; S. Potin et al.
 286 2020). In Figure 5, we show the modeling of the various components of the broad spectral
 feature at $3 \mu\text{m}$, before and after bombardment by He^+ . This EMG modeling is first applied to
 288 spectra from Rubino et al. (2020), that we acquired with an Agilent Cary 670/620 micro-
 spectrometer installed at the SMIS beamline of the SOLEIL synchrotron (France), using a
 290 Schwarzschild objective with a numerical aperture of 0.81. We measured IR spectra using the
 internal Globar source, with respect to gold references, following the same procedure described
 292 by (Brunetto et al. 2018). Spectra were baseline-corrected and normalized using a linear
 continuum between 2.6 and $4 \mu\text{m}$.

294



296 Figure 5. Comparison of the components forming the band at $3 \mu\text{m}$ before and after ion implantation on a pellet of Serpentine Rawhide, measured on an IR micro-spectrometer using Schwarzschild objective with a numerical

298 aperture of 0.81. The values are normalized considering a linear continuum around the absorption band. Fitting
values from EMG modeling and their associated errors are shown in table C1 in Appendix C.

300

The high spectral resolution (4 cm^{-1}) and dense spectral sampling of these
302 measurements allow the precise detection of various components in the band. The large
absorption band at $3\text{ }\mu\text{m}$ is a combination of several features, each tracing the presence of a -
304 OH group bearer, plus the nearby features around $3.4\text{ }\mu\text{m}$ due to $-\text{CH}_2$ and $-\text{CH}_3$ aliphatic
groups. The various detected components could be due to a metal-OH group in a hydrated
306 mineral, or water molecules. Variations in band depth, position of the minimum and FWHM
are the results of modifications in the number of hydroxyl groups, as well as in the crystal
308 structure of the minerals, as shown by previous investigations (Bishop et al. 1994, Frost et al.
2000, Kuligiewicz et al. 2015, Potin et al. 2020b). A shift upon ion-bombardment in the
310 position of the minimum and/or broadening of the band with respect to the non-bombarded
sample may indicate a distortion of the crystal lattice, bringing the -OH groups closer or further,
312 so modifying their oscillation frequency. Band depth, position of reflectance minimum, and
Full-Width at Half Maximum (FWHM), for the complete band and each component before and
314 after bombardment, can be found in Appendix C.

It is important to note that the profile of the global band observed on both measurements
316 is still recognizable between the two measurements, with the band depth only augmented by
0.8%, a band position shift of 20 nm toward the longer wavelengths and a decrease of the
318 FWHM of 8 nm upon ion-bombardment. However, the various components of the spectral
feature can be highly altered, such as the metal-OH component at $2.715\text{ }\mu\text{m}$, losing 9% of
320 depth, shifting of 105 nm toward the longer wavelengths and thinning of 17 nm. It is relevant
to keep in mind that the components identification in the case of the ion-bombarded sample
322 can be complicated by the disordering induced by the ion-implantation and the fact that the
spectra associated to the bombarded sample is probably a mix of both bombarded and non-
324 bombarded sample.

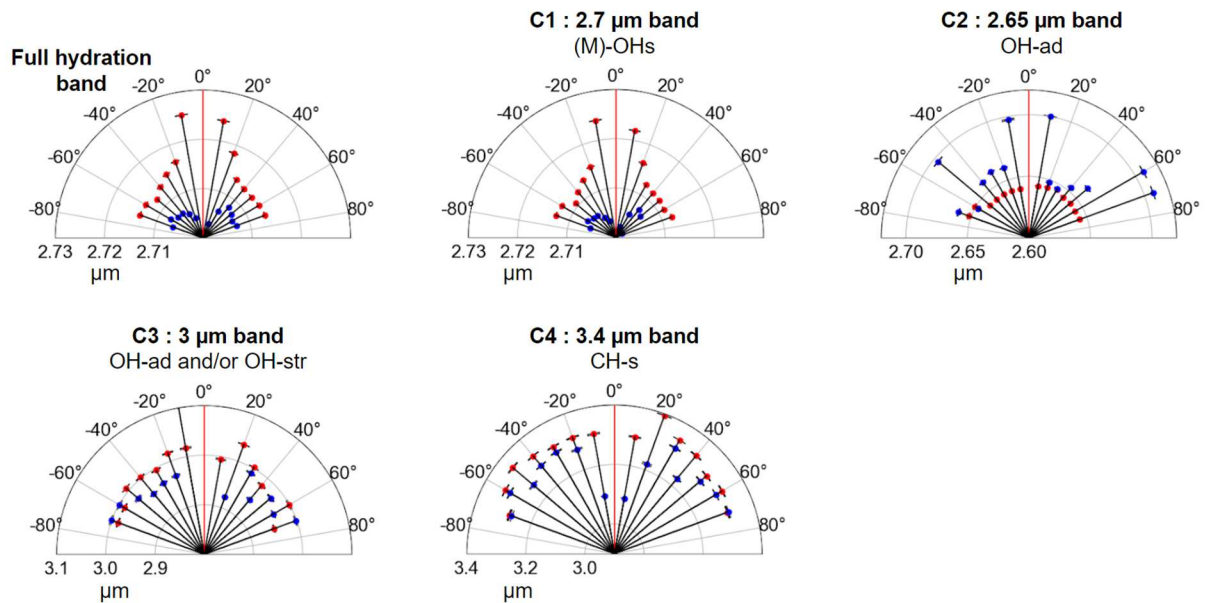
326 Based on the results of the EMG algorithm on the microspectrometer data, we applied
EMG modeling to the REFF measurements. However, since REFF measurements have a lower
328 spectral sampling and resolution than the spectra acquired with the microspectrometer, the
algorithm is able to separate and quantify only four components, some being the combination
330 of the previous detected components too close to each other to be accurately separated with
this spectral resolution and sampling. The components are:

- 332 ❖ C1 : the 2.7 μm peak due to the (M)-OH stretching ;
- ❖ C2 : a small peak at 2.65 μm due to adsorbed water ;
- 334 ❖ C3 : a 3 μm band associated with adsorbed water ;
- ❖ C4 : a band at 3.4 μm due to CH-stretching of organics.

336

The results for the He^+ implanted pellet for illumination angle $i = 0^\circ$ are shown in
 338 Figure 6. We decided to show only the results from the He^+ -implanted pellet, since we already
 saw that the Ar^+ case show little to no spectral changes upon ion bombardment. As a reminder,
 340 we are focusing on the changes in position of the hydration feature since the primary focus of
 this study is to determine possible compositional biases in the interpretation of the hydration
 342 feature's position. This value is representative of the type of hydrated silicate, while other
 parameters - such as band-depth of FWHD - instruct us about ion-implantation effects, such as
 344 amorphization.

346



348 Figure 6. EMG fitting results on the He^+ implanted pellet in red and for the native pellet in blue, for the
 illumination angle $i = 0^\circ$: evolution of the position of the hydration band and of the four components found by
 350 the model. C1= (M)-OH ; C2 = adsorbed-water (OH-as) ; C3 = adsorbed- and structural-water (OH-ad and OH-
 str) ; C4 = organics (CH-stretching) .

352

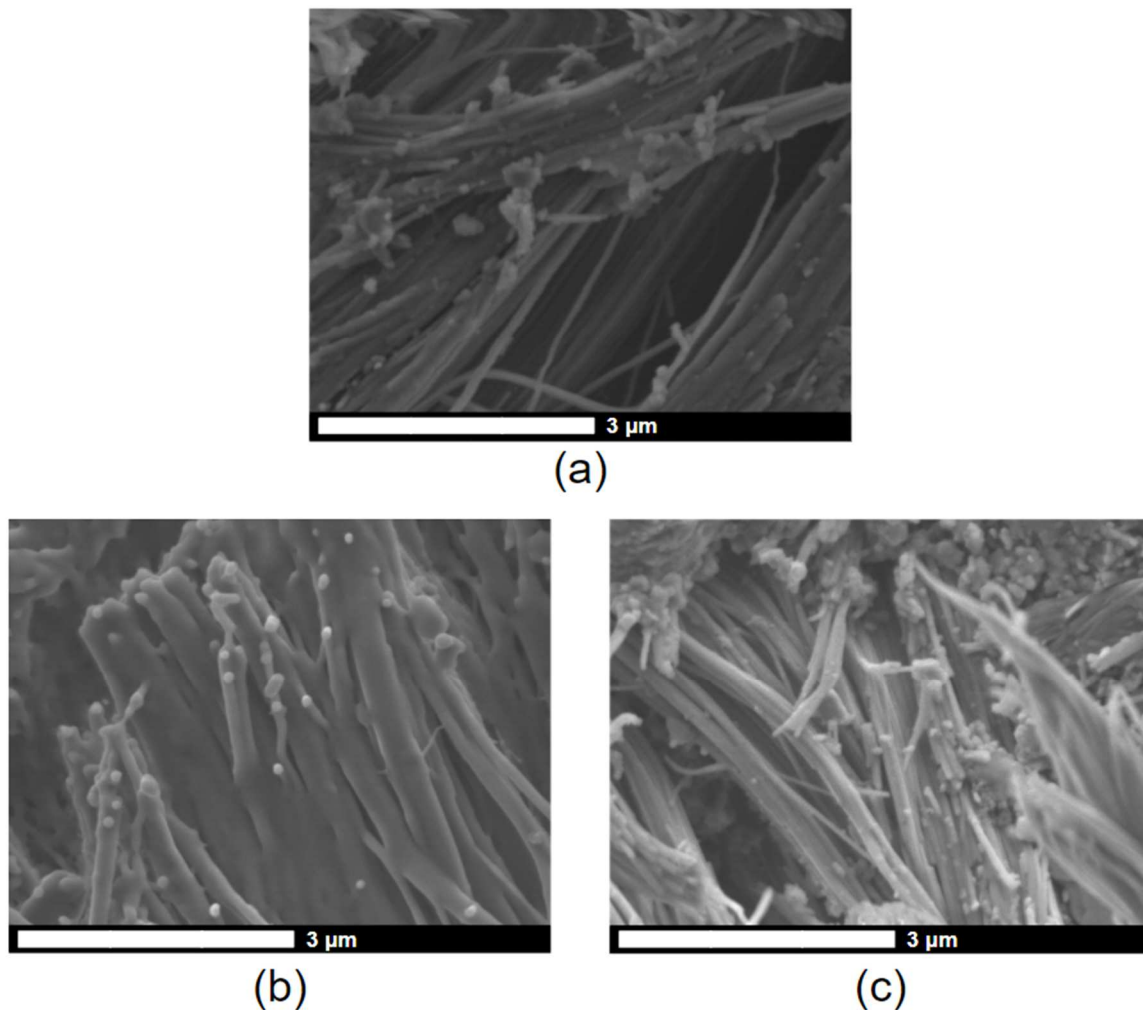
354 We observe that each component is somehow impacted by the irradiation and shows
 different bidirectional behaviors with respect to the non-bombarded sample. However, the

356 changes in the position of the hydration band as a whole are dominated by the shift in position
the $2.7 \mu\text{m}$ peak, as this component represents the major contribution to this spectral feature.
358 The position of each component shown here are not computed with the barycenter method
described in section 3.2, but are instead a result of the EMG modeling. Note that, since our
360 measurements were performed under air, the components related to the adsorbed water
molecules detected at longer wavelengths are not relevant for the remote sensing implication
362 of this work.

364 3.3 SEM imaging results

To further investigate the difference among the He^+ and Ar^+ implantation effects, we
366 analyzed the state of the pellet's surface after bombardment with Scanning Electron
Microscope (SEM) imaging. The acquired images are presented in Figure 7.

368



370 Figure 7. Scanning Electron Microscopy (SEM) images of the centers from the native Serpentine Rawhide pellet

(a), the Ar^+ bombarded pellet (b) and the He^+ bombarded one (c).

372 Images are acquired at 3kV with $\times 20\,000$ magnification.

374 No notable difference can be seen between the He^+ bombarded surface and the
unirradiated one. However, there is a significant difference between these two and the Ar^+
376 bombarded surface. It appears that, even though the spectroscopic effects of the Ar^+ are difficult
to detect, the heavy ion bombardment significantly alters the surface morphology, acting as a
378 smoothing process, contrary to our He^+ bombarded pellet, which retains its grainy and frothy
texture. The Ar^+ dulls and sometimes removes grainy morphological features that characterize
380 the two other pellets. The removed features appear to be smaller than 10 nm in size. The
smoothing resulting from the Ar^+ bombardment has significantly altered the morphology of
382 the pellet's surface, somewhat reducing the granularity of it.

384 4. DISCUSSION

386 Measurements on the He^+ bombarded pellet showed a clear shift in the position of the
 $2.7\ \mu\text{m}$ feature with respect to the non-implanted pellets as well as some slight broadening (see
388 Figure B.2), consistent with ion-bombardment induced disordering, can also be seen. The
spectral shift is due to chemical and physical changes induced by the ion implantation in the
390 first hundreds of nanometers from the surface. The implantation depth in our samples was
estimated by the SRIM software (Ziegler, Ziegler, and Biersack 2010) to be $0.310 \pm 0.090\ \mu\text{m}$
392 for He^+ . However, we have seen that the amplitude of this spectral shift depends on the optical
configuration of each measurement. Such diversity means that different effects are competing
394 at the same time at different geometries. The scattering processes in a multi-layer compact
structure are inherently complex. Two possible contributions and/or competing effects are
396 volume (multiple) scattering and surface (specular) scattering.

Photons undergoing multiple scattering events in the volume of our sample are more
398 sensible to the deeper layers of our sample. As the illumination angle increases, these photons
will likely probe less deep. However, since the sample is observed at wavelengths of 2-3 μm ,
400 photons do not resolve layering at the scale of the implanted layer (approximately $0.3\ \mu\text{m}$ as
said above), thus mixing up both implanted and non-implanted material. The second
402 contribution is related to specular scattering, which is sensitive to the optical properties of the
utmost top layers of our samples. In specular reflection, the probing depth length would still
404 mix ion-implanted and non-implanted matter, but we can qualitatively expect here to have a

more prominent contribution from the ion-implanted one, compared to volume scattering.
406 Hence, the specular component carries more information about the very top layer. This
explains why specular geometrie in our dataset seem to better relay the effects of the ion-
408 implantation, via the larger measured band-shift. The larger shift measured for $i = 0^\circ$ at near-
specular configuration compared to the other near-specular configurations could be explained
410 taking in account the contribution of backscattered photons, which are also particularly
sensitive to the surface layers of our samples.

412 All the patterns seen in our data may result from the combination of volume scattering,
specular scattering and possibly backscattering. Overall, the observations suggest that
414 measurements at high illumination angles of ion-implanted surfaces in near-specular
configuration will be inherently slightly blue-shifted with respect to measurements done with
416 a smaller illumination angle.

418 As we compare the effects of He^+ and Ar^+ implantation, we see that for the latter the
effects on the hydration feature's position are barely detectable, independently from the optical
420 configuration. The relative thickness of the layers altered by the two ions is noticeably distinct,
as there is an order of magnitude difference between the penetration depth of He^+ and Ar^+ in
422 serpentine (from SRIM code simulation : $\sim 0.310 \mu m$ for He^+ and $\sim 0.040 \mu m$ for Ar^+).
Stopping-power profiles for these two ions, shown in (Brunetto et al. 2014), highlight the
424 different energy-loss behavior, which explain the difference in the penetration depth of our
ions. The SEM images in Figure 7 also highlight that the effects of Ar^+ are more prominent on
426 the pellet's surface. A smaller penetration depth means that there's less implanted/modified
matter to probe. The photon's optical path is dominated by native matter, the thickness of the
428 Ar^+ -implanted layer is much smaller than the wavelength of the probing photon, hence the
difficulty in seeing the spectral effects of implanted matter. The altered layer is poorly relevant
430 even at specular geometry. The light loss of surface granularity, due to Ar^+ sputtering, doesn't
seem to play a particular role here.

432
Our study highlights that there is an optimal way to remotely detect ion implantation
434 effects on Solar System surfaces: the spectral effects on hydrated surfaces can be better
observed near specular configuration with near-nadir illumination angle. Incidence angles
436 between 20 and 40° can also suffice, in case near-specular configuration is not achievable.
These results can be put in the context of the Near-IR spectroscopic surveys carried out on the
438 primitive hydrated bodies Ryugu and Bennu. In terms of remote sensing observation, the

configuration that would maximize the spectral effects of space weathering on a primitive
440 hydrated body would correspond to a measurement performed in nadir configuration (the
detector onboard the orbiting craft is observing perpendicularly to the surface of the studied
442 body) with a small phase angle φ associated with the measurement. However, it is relevant to
point out that for this to work, the asteroidal surface to be analyzed would need to be
444 particularly flat, which is not necessarily the case. For real case objects, surfaces are randomly
distributed in orientation within the orbiter's observation footprint and in many cases are
446 covered by regolith, which means that the specular components can be weaker and more
dispersed than for our flat pellets: its contribution would be less easy to quantify. This sentence
448 however has to be nuanced, since recent sample return missions, both Hayabusa missions and
OSIRIS-REx, have shown that the idea of regolith covering the entirety of the surface of small
450 airless bodies is a notion that needs to be revisited. Light regolith may escape the gravitational
pull of small bodies, or flow and accumulate in certain regions. This means that, in the light of
452 our study, for some geographical region, the specular component (which would always be
present) would possibly be significant enough to carry sensible information for surface
454 composition studies. Moreover, the spectral shift would probably be also more easily detected
in spectroscopic surveys with a tighter field of view, dedicated to some particularly regular
456 feature of interest. This would be the case for example for measurements conducted on fresh
impact craters, boulders or fragments of boulders (which could be fractured due to temperature
458 variations, hence exposing flat surfaces) or for rover/lander based measurements, where the
chances of having the detector pixel filled with a smooth-enough surface would be larger. For
460 now, these effects may be still hidden in the already acquired datasets, since the current trend
consist of comparing different facets of a boulder at the same geometry of observation (see the
462 study of the Otohime Saxon on Ryugu by Tatsumi et al. (2021)), instead of focusing on one
facet at different geometries.

464 In the case of Ryugu and Bennu, their spectroscopic surveys were performed at varying
geometric configurations on various regions. In Bennu's case, Deshapriya et al. (2021) show
466 that crater regions on Bennu display a slightly blue-shifted hydration feature with respect to
the average position of $2.74 \mu\text{m} (\pm 0.01)$ (Hamilton et al. 2019). This effect may point to the
468 presence of less-weathered regions on the surface of Bennu, but in the light of this study, it
would prove relevant to put in perspective these results with information regarding the
470 measurement's geometry used for crater survey. Furthermore, this also means that the average
position of the hydration feature on Bennu, $2.74 \mu\text{m} (\pm 0.01)$ (Hamilton et al. 2019), may be
472 slightly blue-shifted due to the contribution of these blue-shifted regions. Taking into account

474 this blue-shift in the OVIRS band centre would bring its attribution closer to the CI-CM group
2 type spectra described by (Takir et al. 2013), further supporting the CM2.1-2.2 petrologic-
type attribution done by Hamilton et al.

476 In the case of Ryugu, the hydration feature has been extensively studied around the
artificial SCI crater (Eri Tatsumi et al. 2019; Arakawa et al. 2020). Near-nadir configuration
478 with phase angle $\varphi = 31.1^\circ$ to 35.7° was kept during the various descent operations made to
image the crater (Kitazato et al. 2021). Since phase angle was kept almost constant, the data
480 acquired during the spectroscopic surveys of the SCI crater is, according to our findings,
inherently less biased and easier to interpret, meaning that the slight peak variations of the
482 hydration feature when comparing old and excavated terrains were indeed caused by chemical
alterations at the surface, due to space weathering and/or thermal effects.

484 CONCLUSION

486 In order to better understand how the geometry of observation can affect remote sensing
observations of space weathered primitive bodies, we measured the REFF function of He^+ and
 Ar^+ bombarded serpentine pellets, at varying illumination angles. We found that in the case of
490 the He^+ bombarded, the position of the $2.7\ \mu m$ hydration band, due to the stretching of hydroxyl
groups connected to a metallic cation ((M)-OHs), shifts towards longer wavelengths as we
492 approach specular configuration. This is due to chemical and physical changes induced by ion
implantation effects in the first hundreds of nanometers, such as preferential amorphization of
494 Mg-rich phyllosilicates or preferential sputtering of Mg (Hapke, Cassidy, and Wells 1975).
The larger band-shift is measured at specular configuration, suggesting that the spectral
496 signature of the implanted layer is carried by specular reflection. The diversity in the observed
amplitude of the shift means that the main driver of this effect is the amount of specular
498 reflection in the collected signal. Additional scattering effects will concur to the final result,
but their contribution is more difficult to assess. Using a spectral deconvolution based on EMG
500 profiles, we showed that the irradiation affects the various components of the hydration band
independently. One can suggest that the variation of the band observed on the REFF
502 measurements before and after irradiation are due to the alterations of the components
themselves. Since the $2.7\ \mu m$ hydration band's position is characteristic of the composition of
504 hydrated silicates, it is relevant to highlight its dependency with the angle of measurement, in
order to avoid possible detection and interpretation biases.

506 A future work, currently in preparation, will focus on delving deeper in our sample, in
order to study the chemical and physical changes induced by ion bombardment, using
508 Transmission Electron Microscopy (TEM) imaging and Energy Dispersive Spectroscopy
(TEM-EDS) to investigate the structural and chemical changes of the ion implanted samples.

510

ACKNOWLEDGMENTS

512

We thank O. Mivumbi, D. Ledu, C.O. Bacri, and P. Benoit-Lamaitrie for help and technical
514 support with SIDONIE and INGMAR. INGMAR is a joint IAS-CSNSM (Orsay, France)
facility funded by the P2IO LabEx (ANR-10-LABX-0038) in the framework Investissements
516 d’Avenir (ANR-11-IDEX-0003-01). We would also like to thank A. Fadel for help and
technical support with the SEM acquisitions. Finally, we thank both reviewers from the journal
518 for their precious comments and questions. This work has been funded by the ANR project
CLASSY (Grant ANR-17-CE31-0004-02) of the French Agence Nationale de la Recherche
520 and by the Centre National d’Etudes Spatiales (CNES-France). The instrument SHADOWS
was funded by the OSUG@2020 Labex (Grant ANR10 LABX56), by ‘Europlanet 2020 RI’,
522 within the European Union’s Horizon2020 research and innovation program (Grant N°654208)
and by the Centre National d’Etudes Spatiales (CNES). HL thanks I-SITE ULNE and the MEL
524 for funding. The electron microscopy works at the University of Lille were performed with the
support of the Chevreul Institute, the European FEDER and Région Hauts-de-France.

526

528

530

532

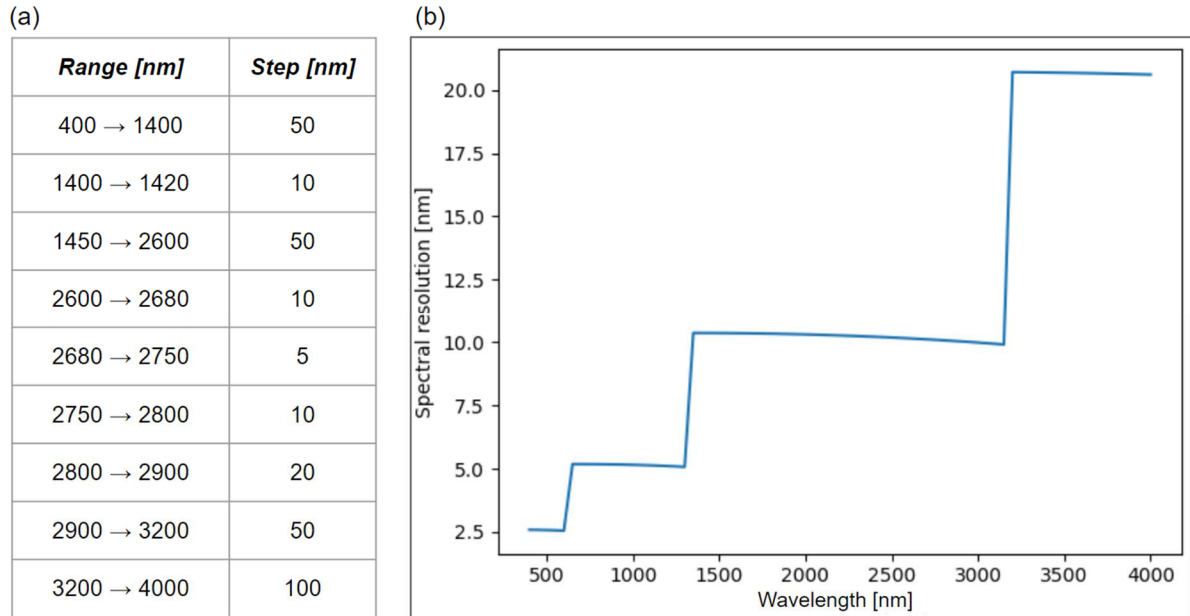
534

536

APPENDIX A : SPECTRAL PARAMETERS

538 The spectral sampling for the acquired spectra was adjusted to be denser around the 2.7
 μm band and looser where there were no bands of interest, to achieve a good compromise

540 between quality of the measurement and time of acquisition. The spectral resolution was also
 542 adjusted with the same intent. In figure A1, both these spectral parameters and their variations
 along the spectra are shown.



544

Figure A1. (a) Evolution of the spectral step and (b) Evolution of the spectral resolution

546

548

550

552

554

556

558

APPENDIX B : COMPLETE REFF DATASET

560

In Figure B1, the complete spectra of the entire REFF dataset for this experiment are shown.

562 For high illumination angles i , when approaching specular configuration, spectral effects due

564 to the domination of the specular components (explained under Figure 1) result in the alteration
of the continuum shape, the reduction of weak features and the accentuation of the 1.4 and the
2.7 μm bands.

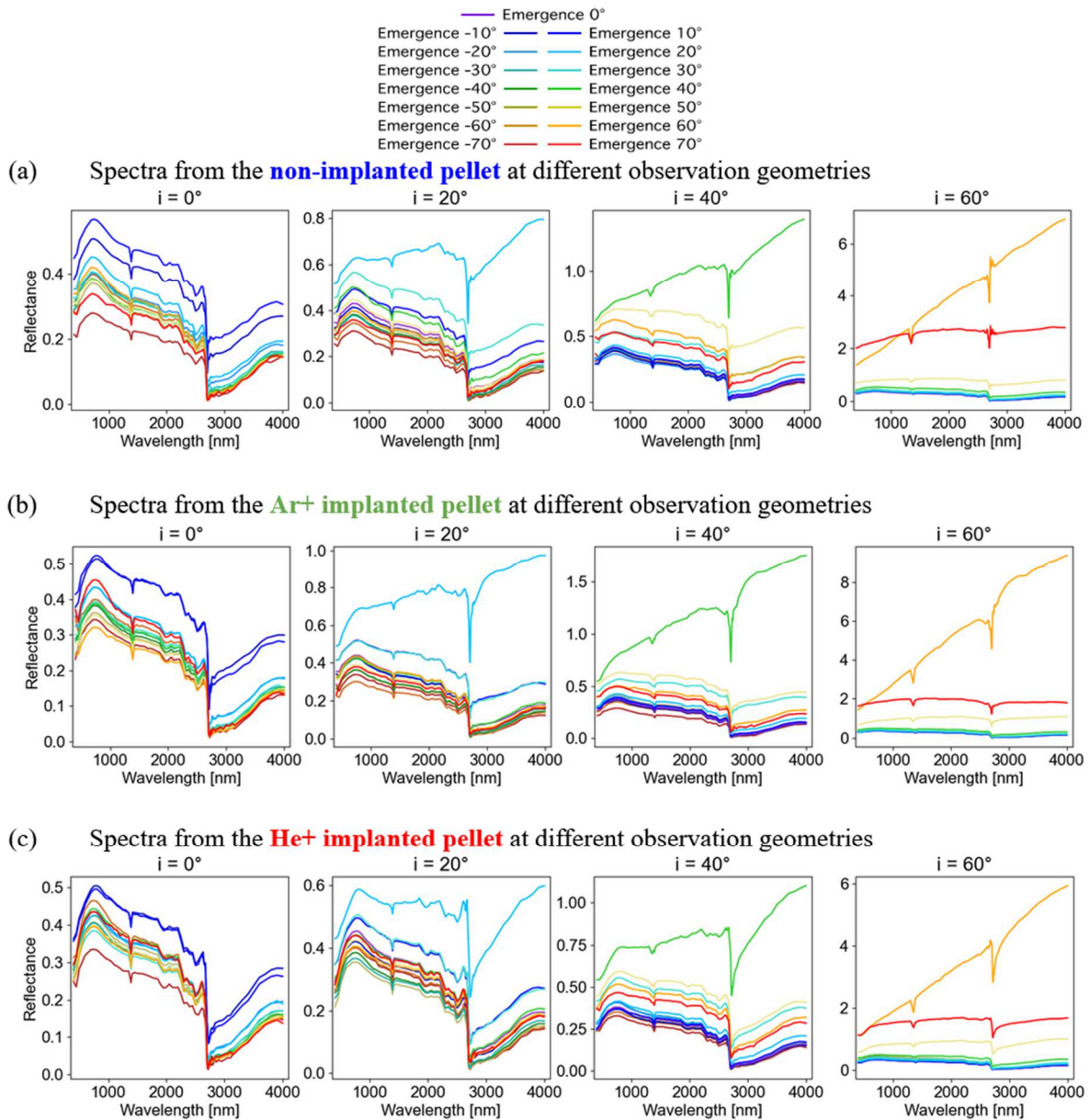


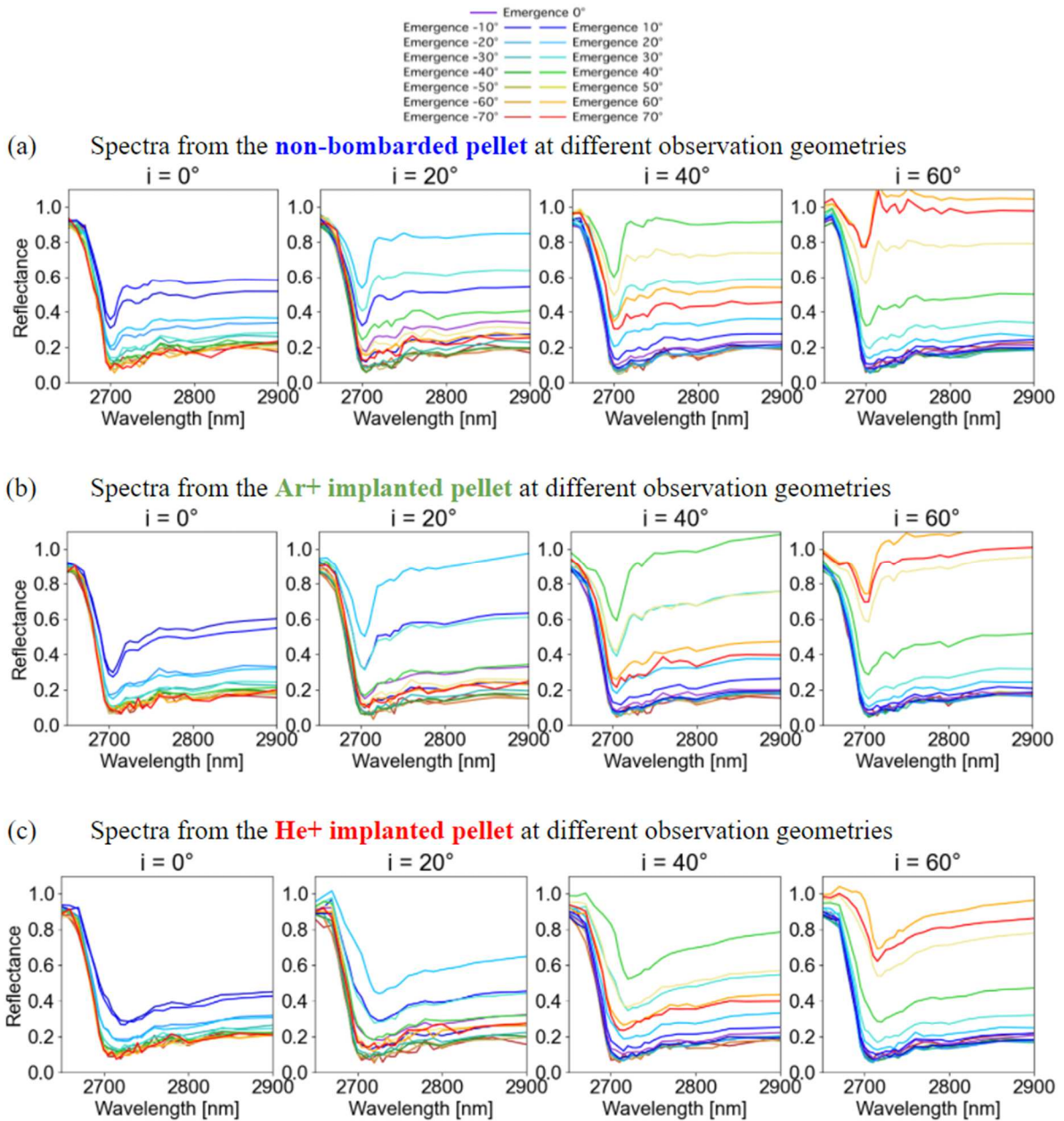
Figure B1. Complete REFF dataset

566

568

In Figure B2, the spectra centered on the hydration feature, after continuum removal, are
shown. We can see that the band tends to shrink as we approach specular configuration. We
are also able to appreciate the change in band-shape and observe the feature broadening upon
ion-implantation, being much wider for the He^+ bombarded sample.

572



574

Figure B2. REFF dataset (complete dataset but restricted to 2.65-2.9 μm , after continuum removal)

576

578

580

582 APPENDIX C : EXPONENTIALLY MODIFIED GAUSSIAN (EMG) MODELING:
 COMPLETE BAND PARAMETERS TABLE

584

Table C1 presents the band parameters of the complete band and components derived from Figure 5. The position of the band is considered as the wavelength at which the reflectance is at its minimum value inside the band. The band depth is calculated as $1 - R_{\text{Band}}/R_{\text{Continuum}}$, at the wavelength corresponding to the center of the band, and considering a linear continuum between the two inflection points of the band, R_{Band} being the measured reflectance at the position of minimum and $R_{\text{Continuum}}$ the reflectance of a linear continuum at the same wavelength. The errors are calculated following the procedure described in Potin et al. (2020a), considering 0.001 error bars and 500 simulated spectra. The errors are calculated, as described in Potin et al. (2020), based on the bootstrap statistical method. In this case, the fits are reproduced 500 times on the original data where a random fluctuation of 0.001 has been added. This method resulted in a large number of spectral parameters for each component, whose distribution is centered on the most probable value, considered here as the modeled band parameter, and with a FWHM corresponding to the error.

Component	Identification		Band depth (%)	Min. Position (nm)	FWHM (nm)	Effect on BD	Effect on Position	Effect on FWHM
Complete band		Virgin	76.943 ± 0.020	2707.554 ± 0.028	617.326 ± 0.246	0,801	20,467	-8,366
		He irradiated	77.744 ± 0.016	2728.021 ± 0.086	608.960 ± 0.220			
1 (light blue)	Water vapor	Virgin	6.264 ± 0.019	2656.891 ± 0.136	58.211 ± 0.756	-1,458	-1,885	-1,42
		He irradiated	4,806 ± 0,043	2655,006 ± 0,117	56,791 ± 1,336			
2 (blue)	metal-OH	Virgin	73.736 ± 0.046	2705.483 ± 0.029	43.838 ± 0.083	-9,497	8,712	91,087
		He irradiated	64,239 ± 1,688	2714,195 ± 0,405	134,925 ± 0,581			
3 (purple)	metal-OH	Virgin	22.422 ± 0.133	2715.049 ± 0.214	168.194 ± 0.293	-9,472	105,478	-17,549
		He irradiated	12,950 ± 0,322	2820,527 ± 0,277	150,645 ± 1,011			
4 (pink)	Water molecule	Virgin	52.393 ± 0.203	2748.566 ± 0.088	126.128 ± 0.079	-34,077	-0,241	14,938
		He irradiated	18,316 ± 1,583	2748,325 ± 0,839	141,066 ± 2,083			
5 (brown)	Water molecule	Virgin	14.578 ± 0.064	2935.286 ± 0.111	205.608 ± 0.299	2,992	-0,702	17,29
		He irradiated	17,570 ± 0,234	2934,584 ± 0,418	222,898 ± 1,576			
6 (orange)	Water molecule	Virgin	31.580 ± 0.058	3084.526 ± 0.202	357.631 ± 0.234	-1,248	7,464	-10,357
		He irradiated	30,332 ± 0,257	3091,990 ± 1,197	347,274 ± 2,112			
7 (green)		Virgin	24.513 ± 0.029	3377.774 ± 0.236	435.971 ± 0.447	0,482	0,337	-10,667
		He irradiated	24,995 ± 0,167	3378,111 ± 2,989	425,304 ± 1,535			
8 (grey)	Organics	Virgin	2.352 ± 0.026	3414.209 ± 0.553	66.581 ± 0.781	0,576	-0,091	6,317
		He irradiated	2,928 ± 0,055	3414,118 ± 0,268	72,898 ± 0,707			
9 (grey)	Organics	Virgin	2.002 ± 0.018	3494.977 ± 0.254	58.211 ± 0.756	0,36	0,786	-1,42
		He irradiated	2,362 ± 0,058	3495,763 ± 0,330	56,791 ± 1,336			
10 (dark green)		Virgin	4.625 ± 0.019	3697.060 ± 0.133	225.406 ± 0.133	0,568	-7,957	12,27
		He irradiated	5,193 ± 0,093	3689,103 ± 01,740	237,676 ± 2,332			

Table C1. Band parameters of the complete 3 μm band and components derived from the modelization shown on Figure 5. The colors to represent the components are similar to those in Figure 5.

REFERENCES

Amma, Shin-Ichi, Jiawei Luo, Carlo G. Pantano, and Seong H. Kim. 2015. "Specular Reflectance (SR) and Attenuated Total Reflectance (ATR) Infrared (IR) Spectroscopy of Transparent Flat Glass Surfaces: A Case Study for Soda Lime Float Glass." *Journal of*

610 *Non-Crystalline Solids* 428 (November): 189–96.

612 Arakawa, M., T. Saiki, K. Wada, K. Ogawa, T. Kadono, K. Shirai, H. Sawada, et al. 2020. “An Artificial Impact on the Asteroid (162173) Ryugu Formed a Crater in the Gravity-Dominated Regime.” *Science* 368 (6486): 67–71.

614 Brunetto, R., C. Lantz, Z. Dionnet, F. Borondics, A. Aléon-Toppani, D. Baklouti, M. A. Barucci, et al. 2018. “Hyperspectral FTIR Imaging of Irradiated Carbonaceous Meteorites.” *Planetary and Space Science* 158 (September): 38–45.

616 Brunetto, R., C. Lantz, D. Ledu, D. Baklouti, M. A. Barucci, P. Beck, L. Delauche, et al. 2014. “Ion Irradiation of Allende Meteorite Probed by Visible, IR, and Raman Spectroscopies.” *Icarus* 237 (July): 278–92.

618 Brunetto, R., C. Lantz, T. Nakamura, D. Baklouti, T. Le Pivert-Jolivet, S. Kobayashi, and F. Borondics. 2020. “Characterizing Irradiated Surfaces Using IR Spectroscopy.” *Icarus* 345 (July): 113722.

620 Brunetto, R., M. J. Loeffler, D. Nesvorný, S. Sasaki, and G. Strazzulla. 2015. “Asteroid Surface Alteration by Space Weathering Processes.” *Asteroids IV*. https://doi.org/10.2458/azu_uapress_9780816532131-ch031.

622 Christensen, P. R., V. E. Hamilton, G. L. Mehall, D. Pelham, W. O’Donnell, S. Anwar, H. Bowles, et al. 2018. “The OSIRIS-REx Thermal Emission Spectrometer (OTES) Instrument.” *Space Science Reviews* 214 (5): 87.

624 Clark, B. E., P. Lucey, P. Helfenstein, J. F. Bell III, C. Peterson, J. Veverka, T. McConnochie, et al. 2001. “Space Weathering on Eros: Constraints from Albedo and Spectral Measurements of Psyche Crater.” *Meteoritics & Planetary Science* 36 (12): 1617–37.

626 Clark, Beth Ellen, Bruce Hapke, Carlé Pieters, and Daniel Britt. 2002. “Asteroid Space Weathering and Regolith Evolution.” *Asteroids III* 585: 90086–90082.

628 Clark, Roger N., Trude V. V. King, Matthew Klejwa, Gregg A. Swayze, and Norma Vergo. 1990. “High Spectral Resolution Reflectance Spectroscopy of Minerals.” *Journal of Geophysical Research* 95 (B8): 12653.

630 De Sanctis, M. C., E. Ammannito, A. Raponi, S. Marchi, T. B. McCord, H. Y. McSween, F. Capaccioni, et al. 2015. “Ammoniated Phyllosilicates with a Likely Outer Solar System Origin on (1) Ceres.” *Nature* 528 (7581): 241–44.

632 Deshapriya, J. D. P., M. A. Barucci, E. B. Bierhaus, S. Fornasier, P. H. Hasselmann, F. Merlin, B. E. Clark, et al. 2021. “Spectral Analysis of Craters on (101955) Bennu.” *Icarus* 357 (March): 114252.

634 Grushka, E. 1972. “Characterization of Exponentially Modified Gaussian Peaks in Chromatography.” *Analytical Chemistry* 44 (11): 1733–38.

636 Hamilton, V. E., A. A. Simon, P. R. Christensen, D. C. Reuter, B. E. Clark, M. A. Barucci, N. E. Bowles, et al. 2019. “Evidence for Widespread Hydrated Minerals on Asteroid (101955) Bennu.” *Nature Astronomy* 3 (4): 332–40.

640 Hapke, B., W. Cassidy, and E. Wells. 1975. “Effects of Vapor-Phase Deposition Processes on the Optical, Chemical, and Magnetic Properties of the Lunar Regolith.” *The Moon*. <https://link.springer.com/article/10.1007/BF00567525>.

642 Ishiguro, Masateru, Takahiro Hiroi, David J. Tholen, Sho Sasaki, Yuji Ueda, Tokuhiko Nimura, Masanao Abe, et al. 2007. “Global Mapping of the Degree of Space Weathering on Asteroid 25143 Itokawa by Hayabusa/AMICA Observations.” *Meteoritics & Planetary Science* 42 (10): 1791–1800.

644 Iwata, Takahiro, Kohei Kitazato, Masanao Abe, Makiko Ohtake, Takehiko Arai, Tomoko Arai, Naru Hirata, et al. 2017. “NIRS3: The Near Infrared Spectrometer on Hayabusa2.” *Space Science Reviews* 208 (1): 317–37.

646 Jones, Thomas D., Larry A. Lebofsky, John S. Lewis, and Mark S. Marley. 1990. “The Composition and Origin of the C, P, and D Asteroids: Water as a Tracer of Thermal

660 Evolution in the Outer Belt.” *Icarus* 88 (1): 172–92.

662 King, A. J., P. F. Schofield, K. T. Howard, and S. S. Russell. 2015. “Modal Mineralogy of CI and CI-like Chondrites by X-Ray Diffraction.” *Geochimica et Cosmochimica Acta* 165 (September): 148–60.

664 Kitazato, K., R. E. Milliken, T. Iwata, M. Abe, M. Ohtake, S. Matsuura, T. Arai, et al. 2019. “The Surface Composition of Asteroid 162173 Ryugu from Hayabusa2 near-Infrared Spectroscopy.” *Science* 364 (6437): 272–75.

666 Kitazato, K., R. E. Milliken, T. Iwata, M. Abe, M. Ohtake, S. Matsuura, Y. Takagi, et al. 2021. “Thermally Altered Subsurface Material of Asteroid (162173) Ryugu.” *Nature Astronomy*, January. <https://doi.org/10.1038/s41550-020-01271-2>.

670 Lantz, C., R. Brunetto, M. A. Barucci, E. Dartois, J. Duprat, C. Engrand, M. Godard, D. Ledu, and E. Quirico. 2015. “Ion Irradiation of the Murchison Meteorite: Visible to Mid-Infrared Spectroscopic Results.” *Astronomy & Astrophysics*. <https://doi.org/10.1051/0004-6361/201425398>.

672 Lantz, C., R. Brunetto, M. A. Barucci, S. Fornasier, D. Baklouti, J. Bourçois, and M. Godard. 2017. “Ion Irradiation of Carbonaceous Chondrites: A New View of Space Weathering on Primitive Asteroids.” *Icarus* 285 (March): 43–57.

674 Lauretta, D. S., S. S. Balram-Knutson, E. Beshore, W. V. Boynton, C. Drouet d’Aubigny, D. N. DellaGiustina, H. L. Enos, et al. 2017. “OSIRIS-REx: Sample Return from Asteroid (101955) Bennu.” *Space Science Reviews* 212 (1): 925–84.

678 Madejová, J., W. P. Gates, and S. Petit. 2017. “IR Spectra of Clay Minerals.” *Developments in Clay Science*. <https://doi.org/10.1016/b978-0-08-100355-8.00005-9>.

682 Milliken, Ralph E., John F. Mustard, François Poulet, Denis Jouglet, Jean-Pierre Bibring, Brigitte Gondet, and Yves Langevin. 2007. “Hydration State of the Martian Surface as Seen by Mars Express OMEGA: 2. H₂O Content of the Surface.” *Journal of Geophysical Research* 112 (E8). <https://doi.org/10.1029/2006je002853>.

684 Mooney, T., and R. F. Knacke. 1985. “Optical Constants of Chlorite and Serpentine between 2.5 and 50 μm .” *Icarus* 64 (3): 493–502.

686 Müller, Christian Menno, Bobby Pejčić, Lionel Esteban, Claudio Delle Piane, Mark Raven, and Boris Mizaikoff. 2014. “Infrared Attenuated Total Reflectance Spectroscopy: An Innovative Strategy for Analyzing Mineral Components in Energy Relevant Systems.” *Scientific Reports* 4 (October): 6764.

690 Ockman, Nathan. 1958. “The Infra-Red and Raman Spectra of Ice.” *Advances in Physics* 7 (26): 199–220.

694 Potin, Sandra, Olivier Brissaud, Pierre Beck, Bernard Schmitt, Yves Magnard, Jean-Jacques Correia, Patrick Rabou, and Laurent Jocu. 2018. “SHADOWS: A Spectro-Gonio Radiometer for Bidirectional Reflectance Studies of Dark Meteorites and Terrestrial Analogs: Design, Calibrations, and Performances on Challenging Surfaces.” *Applied Optics* 57 (28): 8279–96.

698 Potin, S., P. Beck, B. Schmitt, and F. Moynier. 2019. “Some Things Special about NEAs: Geometric and Environmental Effects on the Optical Signatures of Hydration.” *Icarus* 333 (November): 415–28.

700 Potin, S., S. Manigand, P. Beck, C. Wolters, and B. Schmitt. 2020. “A Model of the 3- μm Hydration Band with Exponentially Modified Gaussian (EMG) Profiles: Application to Hydrated Chondrites and Asteroids.” *Icarus* 343 (June): 113686.

704 Rivkin, A. S., E. S. Howell, F. Vilas, and L. A. Lebofsky. 2002. “Hydrated Minerals on Asteroids: The Astronomical Record.” *Asteroids III* 1: 235–53.

706 Rubino, S., C. Lantz, D. Baklouti, and H. Leroux. 2020. “Space Weathering Affects the Remote Near-IR Identification of Phyllosilicates.” *The Planetary Report*. <https://iopscience.iop.org/article/10.3847/PSJ/abb94c/meta>.

708

- 710 RYSKIN, and Y. I. 1974. “The Vibrations of Protons in minerals:Hydroxyl, Water and
Ammonium.” *The Infrared Spectra of Minerals*, 137–82.
- 712 Takir, Driss, Joshua P. Emery, Harry Y. Mcsween, Charles A. Hibbitts, Roger N. Clark, Neil
Pearson, and Alian Wang. 2013. “Nature and Degree of Aqueous Alteration in CM and
714 CI Carbonaceous Chondrites.” *Meteoritics & Planetary Science*.
<https://doi.org/10.1111/maps.12171>.
- 716 Tatsumi, Eri, Toru Kouyama, Hidehiko Suzuki, Manabu Yamada, Naoya Sakatani, Shingo
Kameda, Yasuhiro Yokota, et al. 2019. “Updated Inflight Calibration of Hayabusa2’s
718 Optical Navigation Camera (ONC) for Scientific Observations during the Cruise Phase.”
Icarus 325 (June): 153–95.
- 720 Tatsumi, E., C. Sugimoto, L. Riu, S. Sugita, T. Nakamura, T. Hiroi, T. Morota, et al. 2021.
“Collisional History of Ryugu’s Parent Body from Bright Surface Boulders.” *Nature*
722 *Astronomy* 5 (1): 39–45.
- Usui, Fumihiko, Sunao Hasegawa, Takafumi Ootsubo, and Takashi Onaka. 2018.
724 “AKARI/IRC near-Infrared Asteroid Spectroscopic Survey: AcuA-Spec.” *Publications*
of the Astronomical Society of Japan 71 (1). <https://doi.org/10.1093/pasj/psy125>.
- 726 Watanabe, Sei-Ichiro, Yuichi Tsuda, Makoto Yoshikawa, Satoshi Tanaka, Takanao Saiki, and
Satoru Nakazawa. 2017. “Hayabusa2 Mission Overview.” *Space Science Reviews* 208
728 (1): 3–16.
- Ziegler, James F., M. D. Ziegler, and J. P. Biersack. 2010. “SRIM – The Stopping and Range
730 of Ions in Matter (2010).” *Nuclear Instruments and Methods in Physics Research*
Section B: Beam Interactions with Materials and Atoms.
732 <https://doi.org/10.1016/j.nimb.2010.02.091>.

734